Effect of PCBM additive on morphology and optoelectronic properties of P3HT-*b*-PS films

Rui Wang [a, b, *], Zhen-Yu Di [a], Peter Müller-Buschbaum [b], Henrich Frielinghaus [a]

[a] *Jülich Centre for Neutron Science (JCNS) at Heinz Maier-Leibnitz Zentrum (MLZ), Forschungszentrum Jülich GmbH, Lichtenbergstr. 1, 85748 Garching, Germany. E-mail: r.wang@fz-juelich.de*
[b] *Physik-Department, Lehrstuhl für Funktionelle Materialien, Technische Universität München, James-Franck-Str. 1, 85748 Garching, Germany*

Abstract

Thin blend films of the diblock copolymer poly(3-hexylthiophene-2,5-diyl)-*block*-polystyrene (P3HT-*b*-PS) and phenyl-C61-butyric acid methyl ester (PCBM) are prepared and investigated. The morphology of films with 9, 25, 33, 50, 58 and 67% PCBM weight fraction is determined. The surface topography is probed with optical microscopy and atomic force microscopy whereas the lateral inner structures are determined using grazing incidence small angle neutron scattering (GISANS). Grazing incidence X-ray diffraction (GI-XRD) shows a blend ratio dependence of the P3HT crystallites orientation within the block copolymer films. The thermodynamically favoured P3HT edge-on orientation is suppressed upon increasing the PCBM content from 9% till 33% while it recovers in samples with a PCBM weight fraction above 50%. PCBM tends to interact with the PS block at low PCBM fractions and forms segregated domains at a PCBM weight fraction higher than 50%. The addition of PCBM decreases the degree of lamellar structure order and well-ordered hexagonal packed cylindrical structures emerge in at a PCBM weight fraction of 67%. Absorbance and photoluminescence measurements show the relationship between morphology transformation and optoelectronic properties. The phenomena reported here could provide an alternative view for potential nanotechnology applications.

Keywords: block copolymer, self-assembly, morphology, GISANS

Highlights:

- The morphology and optoelectronic properties of P3HT-*b*-PS:PCBM blend films are studied.
- GISANS reveals a morphology transformation from a lamellar morphology into a hexagonally packed cylinder morphology.
- The addition of PCBM perturbs the crystallization of the P3HT block.
- Enhanced microphase separation of P3HT-*b*-PS is found at a PCBM weight fraction above 50%.
- The shift in morphology directly impact on the charge carrier transportation in the blends.

Graphical abstract

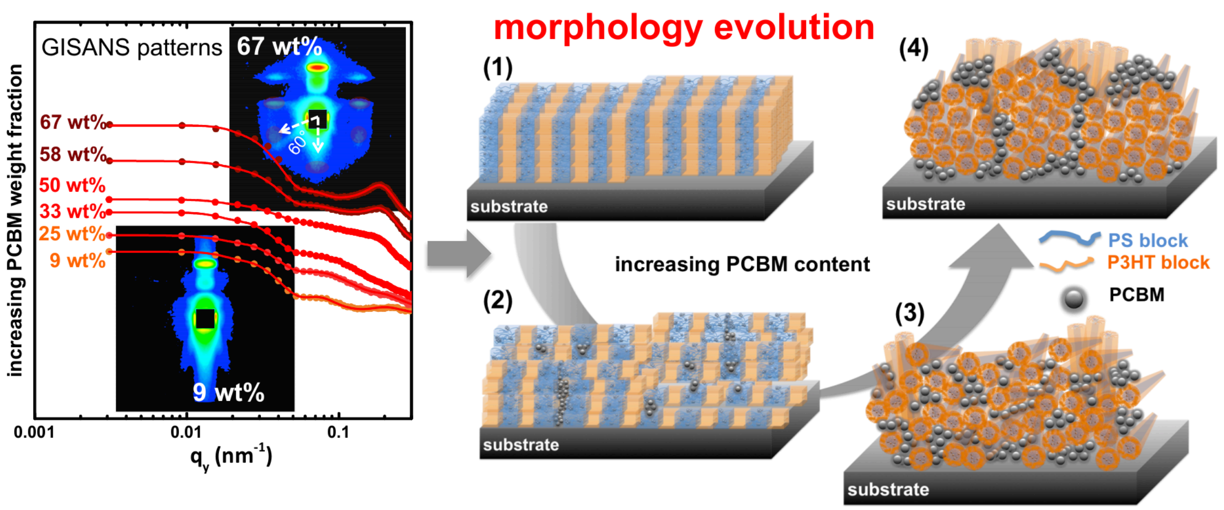

---

* Corresponding author.
E-mail: r.wang@fz-juelich.de (R. Wang).

1. Introduction

Block copolymers are a very promising material due to its intrinsic ability to microphase separate into a variety of well-defined nanostructures via self-assembly.[1-3] Instead of blending two immiscible polymers, which commonly results in macrophase separation, both polymers are covalently connected thereby forming a diblock copolymer. Thus, macrophase separation is prevented and the inter-block incompatibility drives the formation of an array of highly ordered nanostructures.[4,5] As a consequence, the generated fine patterns have manifested such diblock copolymers to be very promising for the functional nanotechnology applications, as for example in electronics, for batteries, medical drug delivery and as membranes.[6-11]

Among the classical model systems for diblock copolymers, numerous studies have focused on coil-coil block copolymers.[4,12,13] In principle, the nanostructuring in coil-coil block copolymers is determined by the Flory-Huggins interaction parameter χ, the total degree of the polymerization N and the volume fraction parameter f of the blocks.[14-16] However, besides the rather well studied coil-coil block copolymers also rod-coil block copolymers have gained increasing interest. In rod-coil block copolymers the conjugated block can offer unique optoelectronic properties for many potential microelectronic applications. As compared with coil-coil block copolymer, rod-coil block copolymers are more rigid. The rigidity of the rod-coil block copolymers is generated by the conjugated backbone and by the interactions between the aromatic monomers. As a consequence, rod-coil block copolymers exhibit a distinctly different self-assembly behaviour as compared with the conventional coil-coil block copolymers. For rod-coil block copolymers another three important parameters need to be concerned: the Maier–Saupe (π-π) interaction parameter μ, the competition between μ and χ, and the stiffness asymmetry parameter that resulted from the rod to coil length ratio υ.[15-18] Among the various types of rod-coil block copolymers in particular p-type semiconducting conjugated polymers such as poly(3-hexylthiophene) (P3HT) based rod-coil diblock copolymers have attracted high expectations. The P3HT block exhibits intriguing optical and electronic properties which are needed for applications whereas the other block brings additional functionalities in the system.[19-23] The potential of morphology control on the nanometer scale is for example of special interest for applications in organic solar cells. For P3HT typical exciton diffusion lengths are of about 10 nm which is a scale that can be well addressed with block copolymers.[20,24-26]

For solar cell applications besides the p-type semiconductor also an n-type partner is required, which for P3HT is commonly phenyl-C61-butyric acid methyl ester (PCBM). As a consequence, block copolymers with a P3HT block mixed with PCBM have gained interest. For example, Dattani et al. reported the nanostructure morphology evolution in the P3HT-*block*-poly(3-(2-ethylhexylthiophene)) (P3HT-*b*-P3EHT):PCBM blend system. It was revealed that the PCBM composition affects the crystalline fraction of P3HT. However, the nanoscale morphology turned from ordered lamellar into disordered at higher PCBM content.[27] The influence of PCBM on self-assembly of P3HT-*block*-poly(4-vinyl-pyridine) (P3HT-*b*-P4VP) was studied as well. It was reported that PCBM enhances the block copolymer microphase separation and no evidence of crystallize PCBM was observed.[28] In a further example, Lin et al. reported in the poly(3-hexylthiophene)-*block*-poly[3-(2,5,8,11-tetraoxadodecane)thiophene] (P3HT-*b*-P3TODT):bis-[6, 6]-phenyl C61-butyric acid (bis-PCBA) blend film, bis-PCBA prefers to interact with the amorphous P3TODT blocks via hydrogen bonds. As a consequence, macrophase separation of the fullerenes is suppressed and the solar cell devices exhibit enhanced thermal stability with respect to the reference P3HT-b-P3TODT:PCBM blend system.[29]

In the present work, we follow an alternative approach by using a block copolymer with a conjugated, p-type conducting block and blending this with the n-type fullerene derivate to from bulk heterojunction (BHJ) thin films. As a first step, we focus on the morphology and optoelectronic properties of thin blend films of the diblock copolymer P3HT-*block*-polystyrene

(P3HT-*b*-PS) with PCBM. PCBM is blended with P3HT-*b*-PS at various blend ratios. We determine the morphology with atomic force microscopy (AFM), grazing incidence X-ray diffraction (GI-XRD) as well as grazing incidence small angle neutron scattering (GISANS), whereas the optoelectronic properties are studied with UV-Vis spectroscopy and photoluminescence. Such studies will enable to select promising candidates to be further processed into optoelectronic devices in future. The obtained results show that the self-assembly of the diblock copolymer is strongly influenced by the addition of PCBM. The intermolecular orientation of P3HT crystallites alters alongside with the PCBM concentration. Interestingly, a well-organized hexagonally packed cylinder morphology of P3HT-*b*-PS emerges above a specific PCBM weight concentration. All observed structures distinctly affect the optoelectronic properties of the active layer.

2. Experimental

2.1 Sample preparation

Poly(3-hexylthiophene-2,5-diyl)-*block*-polystyrene (P3HT-*b*-PS) and phenyl-C61-butyric acid methyl ester (PCBM) were purchased from Polymer Source, Inc. and 1-material, respectively. Materials were used without further purification. P3HT-*b*-PS has a number average molecular weight of Mn = 12.5-*b*-11.6 (kg mol^{-1}) and a polydispersity index (PDI) of 1.4. Both, P3HT-*b*-PS and PCBM were dissolved in 1,2 – dichlorobenzene at 60 °C overnight with different blend ratios (PCBM weight fraction of 9%, 25%, 33%, 50%, 58%, 67%). Films were prepared via spin coating on acidic pre-cleaned substrates,[30] followed by a thermal annealing at 140 °C for 20 min. By adapting the solution concentration, a constant film thickness of around 120 ± 20 nm was revealed from X-ray reflectivity (XRR) analysis (see supporting information, Fig. S1). On the basis of literature[23-26], we assume that the deposited films have the same composition as compared to the initial solution.

2.2 Surface imaging techniques

The optical microscopy images were obtained with an Axiolab A microscope (Carl Zeiss) combined with a PixelLink USB Capture BE 2.6 CCD camera. Different magnifications from 1.25 X to 100 X were applied to probe the surface in the length scale of several micrometers. The present optical microscopy images were acquired at a magnification of 50 times to secure both statistical relevance and optimum resolution. Atomic force microscopy (AFM) measurements were obtained with Keysight 5500 Scanning Probe Microscope in intermittent contact mode in air. An aluminum backside coated pyramidal silicon tip with a radius around 8 nm, mounted on a cantilever was used. The AFM data were taken with a scan size of 1 μm × 1 μm on exactly those samples used in the GISANS study. Surface route-mean-square (rms) roughness and the power spectral density (PSD) were determined for a quantitative analysis. The PSD yielded lateral, characteristic structure information which can be compared with the scattering data.

2.3 Grazing incidence small angle neutron scattering (GISANS)

GISANS measurements were performed at the KWS-1 instrument at MLZ (Maier-Leibnitz Zentrum), Garching, Germany.[31,32] The collimation length and the sample-to-detector distance was set to 8 m and 7.7 m, respectively. An incidence angle of 0.6° was chosen to probe the inner structure of the entire film. A neutron wavelength of 7 Å was used. The neutron scattering signal was collected by a 2D 6Li Anger-type scintillation detector. Horizontal line cuts were performed at the sample characteristic Yoneda peak with the software QtiKWS. Subsequently, a home-developed software was used to model the extracted scattering intensities by applying two cylinder like lateral structure contributions within the distorted wave Born approximation (DWBA).

2.4 Grazing incidence X-ray diffraction (GI-XRD)

GI-XRD measurements were performed on the PANalytical Empyrean X-ray Diffractometer. The incidence angle was set to 0.2° and the diffraction intensities were recorded along the direction normal to the film surface. Each sample was measured for 17 hr to achieve sufficient statistics.

2.5 Spectroscopic characterization

The UV/Vis absorption spectra were taken with a PerkinElmer UV/vis spectrometer Lambda 35 in a wavelength range from 280 to 1100 nm in transmission geometry. The measurements were carried out under ambient conditions. The photoluminescence data were obtained with a PerkinElmer LS55 fluorescence spectrometer equipped with a red-sensitive detector. Samples are excited at a wavelength of 485 nm and the spectra were recorded in the wavelength range from 550 to 900 nm.

3. Results and discussion

3.1 Surface structures

As shown in the optical microscopy images (Fig. 1), a uniform surface structure is achieved on the micrometer scale for all P3HT-*b*-PS:PCBM films irrespective of the different blend ratios. Distinct clusters are revealed for all samples, which are attributed to the PCBM agglomerates formed upon thermal annealing.[33,34] Alongside the increasing PCBM weight fraction, the clusters are gradually transforming from bright spots (Fig. 1a) into dark crystals (Fig. 1b-c) due to the increased crystal thickness. Above a PCBM weight fraction of 33%, these dark crystals grow in size and large crystals bigger than 10 μm arise (Fig. 1d-f). Notably, distinct PCBM-depletion areas are also apparent in samples 58% (Fig. 1d) and 67% (Fig. 1e) because PCBM crystals grow up and stick out of film plane, leading to a thinner surrounding area.[33] In Fig. 1f big flower-like PCBM crystals are found for the PCBM weight fraction of 67%. A similar structure was reported by Wang et al. in their study about degradation of P3HT:PCBM BHJ blend films prepared from and exposed to different solvents.[21] It was shown that such micrometer-sized aggregates would hamper the photovoltaic device performance.

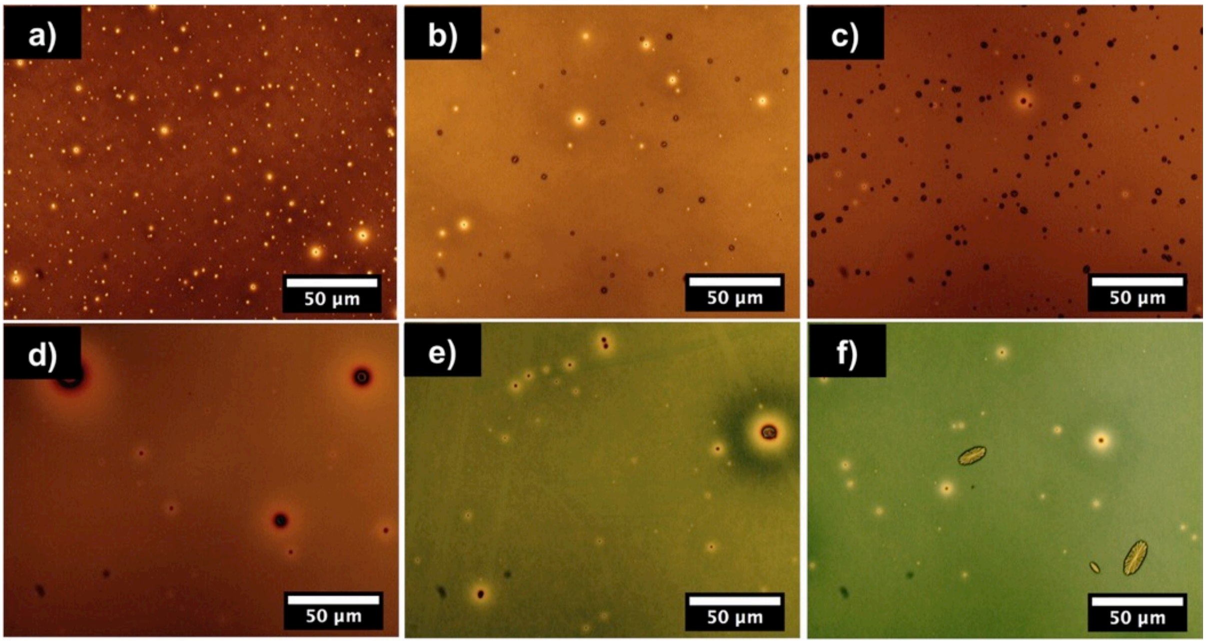

Fig. 1. Optical microscopy images of P3HT-*b*-PS:PCBM blend films with a PCBM weight fraction of (a) 9, (b) 25, (c) 33, (d) 50, (e) 58 and (f) 67%.

Using AFM the local film surface morphology is probed in the nanometer scale. As seen in Fig. 2, the PCBM content has a strong influence on the morphology. For the sample with a PCBM weight fraction of 9% (Fig. 2a), microphase separated randomly distributed lamella-like structures are found which resemble well the morphology of the pure diblock copolymer film (Figure S2 in supporting information). From literature it is evident that these features comprise P3HT rich domains.[27,35,36] Upon further increasing the PCBM concentration up to 33%, these lamellae become less apparent as both, length and width, are diminishing, indicating that the P3HT-*b*-PS self-assembly behavior is affected by the loading with PCBM. Large aggregates around 200 nm appear on the surface (Fig. 2c), which are likely due to the diblock copolymer self-assembly aggregation. For samples with PCBM weight fraction above 50% the lamellae structure is recovered and shows an increased width (Fig. 2d, 2e). At 67% the surface becomes rather featureless with no distinct feature at the applied probing length. For a quantitative analysis, the power spectral density (PSD) curves are calculated in Fig. S3 (see supporting information). Similar to scattering data, the characteristic peaks and shoulders in the PSD curves represent characteristic length scales in the sample. In the PSD of the sample with the lowest PCBM weight ratio (9%), a distinct shoulder is seen in the intensity which shifts towards smaller q values with increasing PCBM content and also becomes less pronounced. Thus, with increasing amount of PCBM the characteristic length scale in the films increases and the corresponding structure becomes less well defined. It is well established that the morphology organization of rod-coil block copolymers containing P3HT segment is driven by both, microphase separation and P3HT crystallization.[37-39] Therefore, further analysis is required to determine the dominant mechanism of the revealed blend morphology seen in the AFM data.

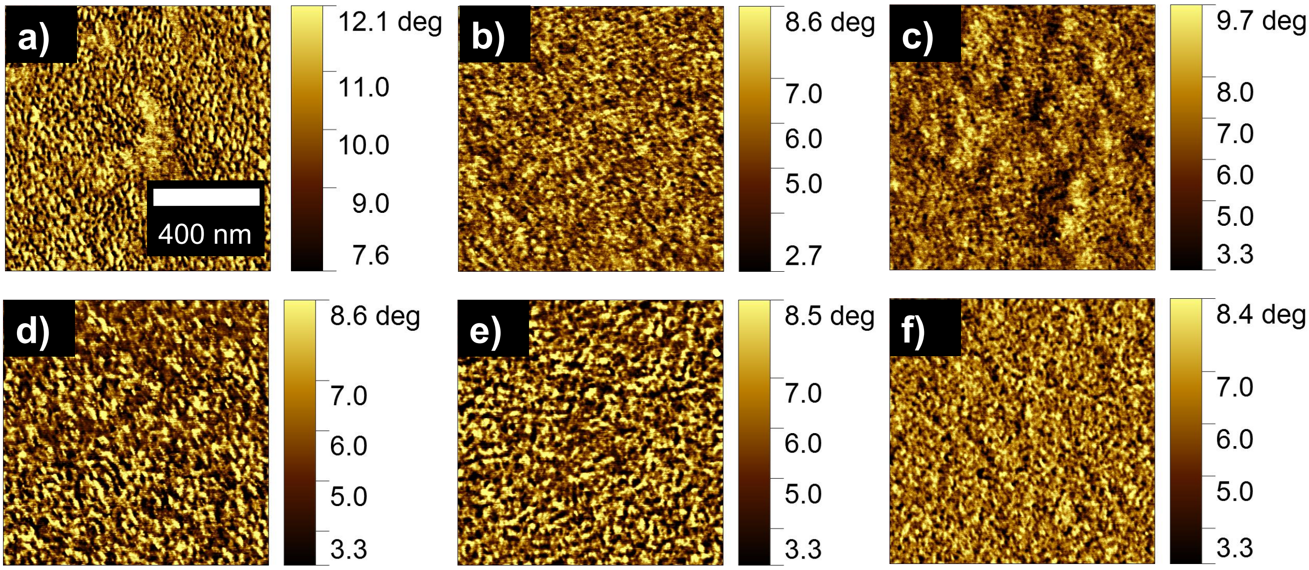

Fig. 2. AFM phase images measured for a scan range of 1×1 μm^2 (scale bar, 400 nm) of P3HT-*b*-PS:PCBM blend films with a PCBM weight fraction of (a) 9, (b) 25, (c) 33, (d) 50, (e) 58 and (f) 67%.

3.2 P3HT crystallites orientation

In order to elucidate the driving mechanism of the resulting morphology in the P3HT-*b*-PS:PCBM blend films, detailed information about the crystalline structure of the blend films is achieved with GI-XRD measurements. The chosen measurement technique was conducted by using a 1D detector to capture the scattering intensities being distributed along the substrate surface normal (nominated as q_z in Fig. 3a). Herein, the results in Fig. 3a represent crystallites which adopt the orientation along the surface normal. As seen in Fig. 3a, the loading of PCBM has distinct effects on the crystallinity and molecular ordering in the composite P3HT-*b*-PS:PCBM films. For the sample with the lowest PCBM weight fraction (9%), the (100) reflection of the P3HT lamellar stacked backbone at $q_z = 3.8$ nm^{-1} and two higher orders, namely the (200) and (300) reflection peaks, are observed, being indicative for a well developed edge-on orientation (depicted in Fig. 3b).[40,41,46] This result suggests that the P3HT block of the block copolymer is not hindered in crystallization, indicating the lamella-structure observed in Fig. 2a is induced by P3HT segment crystallization. In addition no identifiable reflection feature of PCBM crystals is visible for this composition. It was reported that an optimized morphology can be achieved in P3HT:PCBM blends with P3HT-*b*-PS additive, which result from the beneficial impact of a larger interaction energy between PS and PCBM than that of P3HT and PCBM.[44] Therefore, we may hypothesize that the PCBM molecules distribute in the PS segments with a poor degree of crystallization at this composition.

The well pronounced (h00) reflections decrease upon further adding PCBM up to 33% due to a loss in crystalline order whereas another reflection of the P3HT aromatic π-π stacking at $q_z = 16.8$ nm^{-1} appears. Thus, a more kinetically favorable face-on orientation of P3HT crystallites (depicted in Fig. 3c) appears in case of these blend ratios.[41] The addition of nanoparticles or fullerene to a well ordered block copolymer matrix can lead to an entropic penalty together with a segment stretching to accommodate the additive, which create disorder or macrophase-separation.[29,43] Herein, on the basis of the obtained results, we suggest a kinetic rather than thermodynamic mechanism dominates at PCBM weight fractions of 25%

and 33%. However, the (010) reflection peak vanishes upon further increasing the PCBM content. More specifically, higher orders of P3HT (h00) reflection are recovered, which indicate that an increased population of thermodynamically stable edge-on crystals has developed in blend films with a PCBM weight fraction above 33%.[42] Notably, the PCBM diffraction peak located at $q_z = 13.8\ \mathrm{nm}^{-1}$ grows in intensity alongside increasing the PCBM content. Hereby, we can conclude that the P3HT crystallites adopt different orientations with respect to the substrate at different blend ratios and better ordered PCBM crystalline domains emerge in sample containing a higher PCBM content.

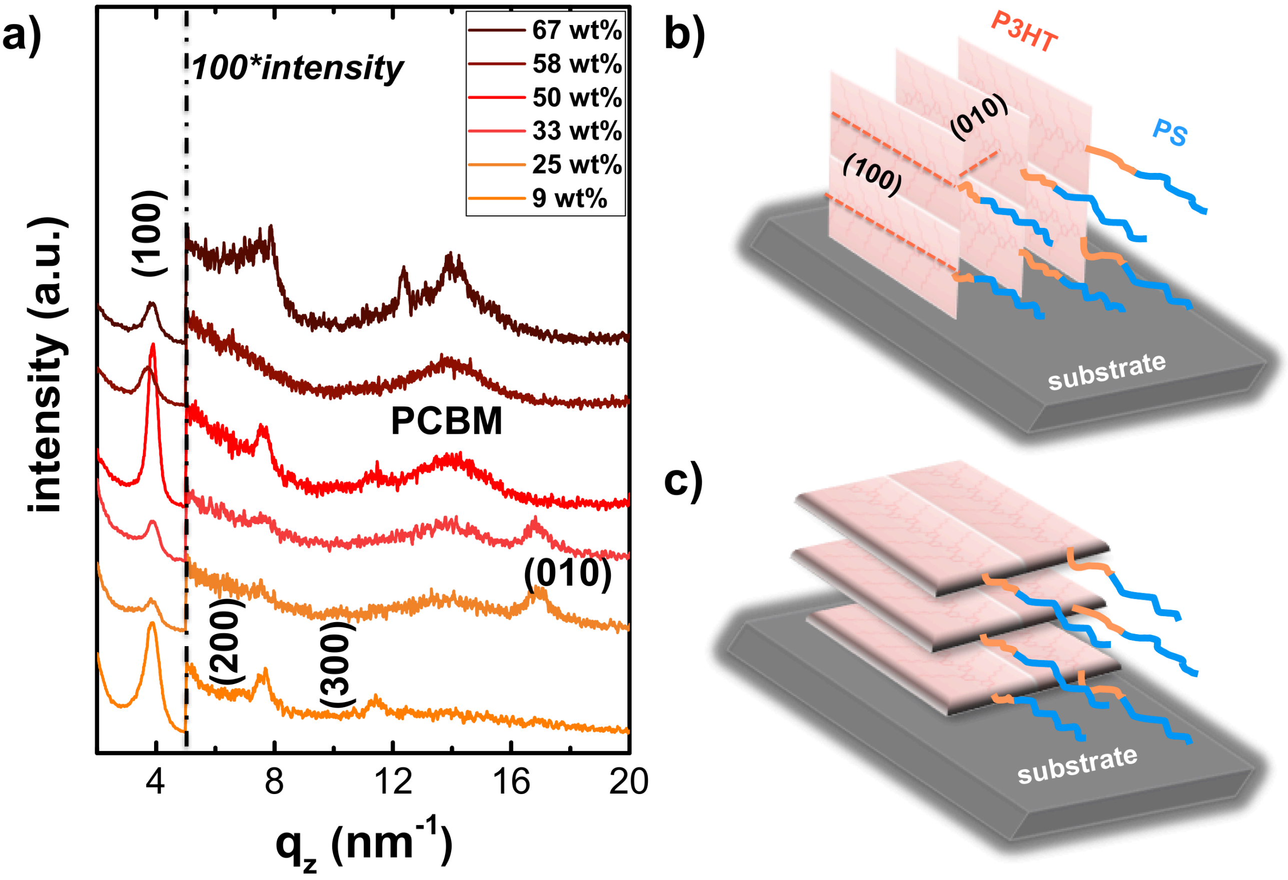

Fig. 3. (a) GI-XRD data of BHJ films with different blend ratios as indicated. For $q_z > 5\ \mathrm{nm}^{-1}$, the intensities are multiplied by a factor 100 to increase visibility of the weak peaks. The curves are shifted along the y-axis for clarity. Schematic illustration of P3HT crystallites with (b) edge-on orientation and (c) face-on orientation.

3.3 Inner lateral structures

In order to understand the mesoscale morphology which is present inside the blend films, all samples are characterized with grazing incidence small-angle neutron scattering (GISANS).[47] In general, grazing incidence small angle scattering (GISAS) using either x-rays or neutrons is well suited to investigate the buried structure of active layers in organic photovoltaic (OPV) devices.[48-53] Besides the surface structure information, GISAS offers the opportunity to examine the inner morphology in terms of lateral structure size distributions and spatial correlations. As a consequence, GISAS is able to probe the copolymer 3D morphology.[54] In the traditional P3HT:PCBM BHJ system, apart from the pure P3HT and pure PCBM phases, a mixed phase between polymer and fullerene was reported.[45,55,56] In particular for neutrons the contrast conditions are beneficial to probe this third phase, which renders GISANS a valuable technique to investigate the system.

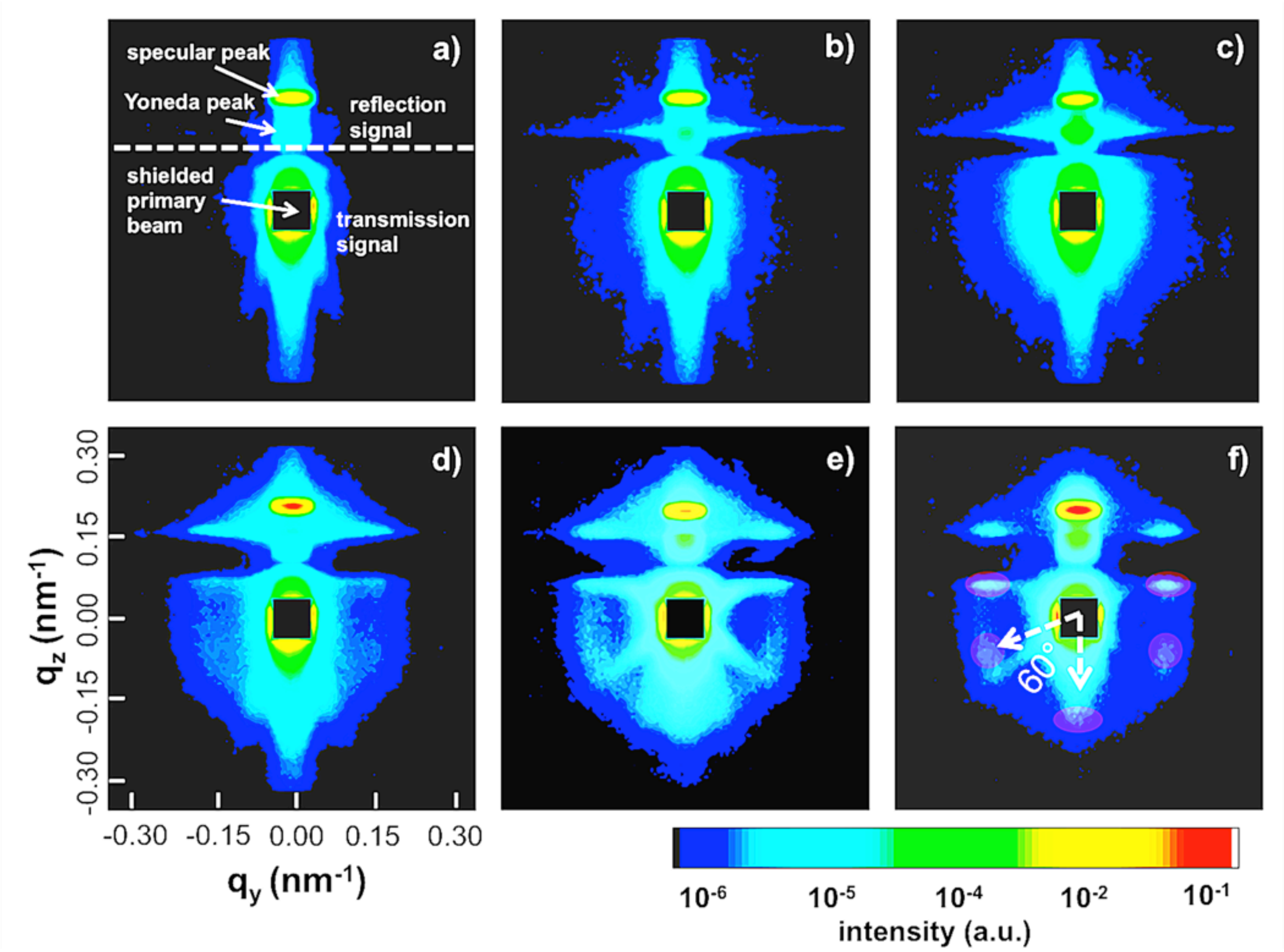

Fig. 4. 2D GISANS data of P3HT-*b*-PS:PCBM blend films with a PCBM weight fraction of (a) 9, (b) 25, (c) 33, (d) 50, (e) 58 and (f) 67%. The silicon substrates are transparent for neutrons and a transmitted intensity is seen below the sample horizon (indicated by the horizontal dashed line in 4a). The components of the scattering vector q_y and q_z represent the directions horizontal and normal to the sample surface, respectively. In 4a characteristic features in the intensity are marked.

The obtained 2D GISANS data are shown in Fig. 4. The intensities are displayed in different colors on logarithmic scale for a better comparison. Since the Si substrates are transparent for neutrons, in addition to the reflected GISANS signal also a transmitted intensity is observed below the sample horizon. Above the horizon two prominent scattering features are seen in the GISANS data. The Yoneda peak is located at small q_z values and the specular peak at higher q_z values due to the chosen incident angle. The Yoneda peak emerges at the critical angle of the investigated material and therefore it is a material-sensitive peak.[57] Yoneda peaks are well apparent for all sample compositions in the measured data. A full set of vertical line cuts along $q_y = 0$ nm^{-1} is displayed for all the six blend films in Fig. 5a. With increasing amount of PCBM in the films the position of the Yoneda peak shifts towards larger q_z values. Because PCBM has a larger neutron scattering length density (SLD) as compared with P3HT-*b*-PS this shift resembles the amount of PCBM embedded in the block copolymer. In addition the shape of the Yoneda peaks changes. A wing-like scattering feature arises from the contrast enhanced nano-scale structure inside the investigated films. At a PCBM weight fraction of 58%, side maxima $q_y \approx 0.2$ nm^{-1} in the wing-like Yoneda peak appear (Fig. 4e), which suggests that the interaction between PCBM and P3HT-*b*-PS promotes the formation of a highly ordered structure. Notably, an identical result is observed in the vertical line cuts (Fig. 5a) as a peak at $q_z \approx 0.2$ nm^{-1} progressively grows in intensity from 50% to 67%. This result suggests that the highly ordered structure not only distribute near the thin film surface but also in the bulk. Moreover, with further increasing the PCBM weigh fraction to 67%, a scattering pattern of hexagonally packed cylinders is revealed in the transmitted scattering signal (Fig. 4f). Due to the limited counting statistics in GISANS, this hexagonal scattering pattern is not observed in the reflection signal. Furthermore, the side peaks are more intensive in the reflected part rather than the transmitted part, illustrating that the hexagonally packed cylinders distribute more close to the film surface. In order to investigate the morphology in the buried thin films, we focus on the scattering signal around the material sensitive Yoneda peak position, by extracting horizontal line cuts from the 2D GISANS data to investigate the lateral domain structures. The obtained cuts are plotted in Fig. 5b.

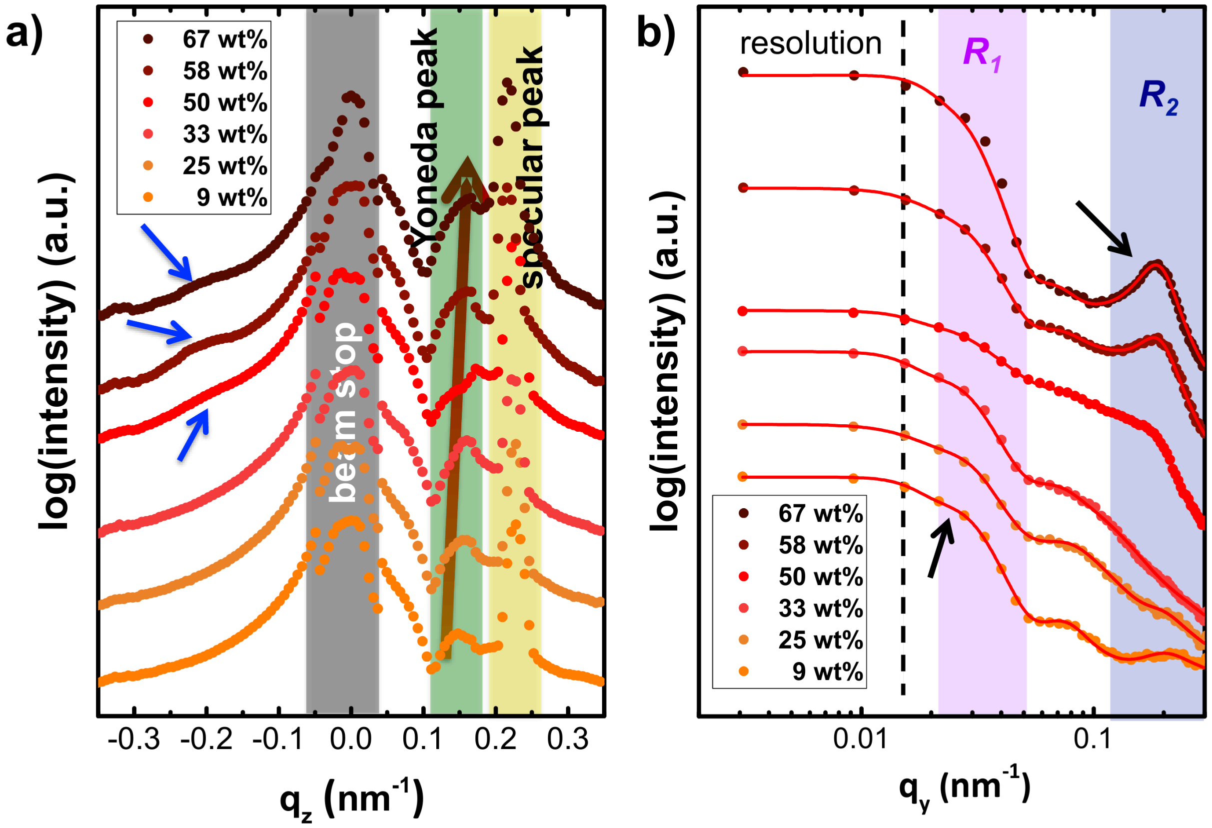

Fig. 5. (a) Vertical line cuts from the 2D GISANS data cut along $q_y = 0$. The direct beam is shielded by a beam stop as indicated by the grey box. The specular peak and Yoneda peak positions are highlight with yellow and green boxes, respectively. The Yoneda peak position shifts towards larger q_z values because PCBM has a bigger neutron scattering length density: $SLD_{P3HT\text{-}b\text{-}PS} = 0.914 \times 10^{-6}$ Å^{-2}, $SLD_{PCBM} = 4.3 \times 10^{-6}$ Å^{-2}. The development of peak at $q_z \approx 0.2$ nm^{-1} at larger PCBM content is highlighted by arrows. (b) Horizontal line cuts along the Yoneda peak positions for samples with the six different blend ratios as indicated. Data are displayed with dots and the fits with red solid lines. Both are shifted along the y axis for clarity of the presentation. The positions of the two substructures are highlighted by arrows and marked as R_1 and R_2 with colored boxes. The resolution limit is indicated with the dashed line.

To estimate the characteristic length scales of the domains, the horizontal line cuts are fitted within the framework of the distorted wave Born approximation (DWBA).[58,59] The extracted results are the best fits obtained by modeling the cuts with two independent cylinder-like substructures distributed over a one-dimensional paracrystal lattice. From this fitting model, form factors referring to the scattering objects and structure factors associated with the spatial distribution of the scattering objects are determined with different size distributions. The extracted morphological parameters on a ten nanometer scale are presented in Fig. 6c with domain size S2 as well as the two respective domain center-to-center distance D2. A full set of the morphological parameter on a hundred nanometer scale is presented in Fig. S6 in the supporting information. Scattering features found between 0.05 nm^{-1} and 0.1 nm^{-1} originate from the Si substrate and are not included in the data analysis.[60] A horizontal line cut of the 2D GISANS data of the pure Si substrate is shown in Fig. S5 (see supporting information) for comparison. It demonstrates that the substrate scattering has no effect on the scattering peaks observed in samples with PCBM weight fractions of 50%, 58% and 67%.

On the mesoscale, a shoulder-like scattering feature is seen in the horizontal line cuts for all samples at $q_y < 0.05$ nm^{-1}. As extracted from the fitting, the corresponding large domains have a size around 120 nm (2 times the domain radius, see Fig. S6 in supporting information). A similar result was reported in case of P3HT:PCBM blend films by Ruderer et al.,[56] indicating that homopolymer and diblock copolymer show a similar in-plane morphology on that large scale. The related averaged scattering intensities of these hundred nanometer domains are plotted in Fig. 6a. Since the scattering intensity is proportional to the square of SLD difference in the blend system (equation S1 in supporting information),[61,62] a decreased average scattering intensity reveals a better mixture of PCBM and the diblock copolymer. Thus, for example if the PCBM weight fraction increases from 33% to 50% (Fig. 6a), a better mixing between the PCBM domain and the diblock copolymer domain on hundred nanometer scale is observed. The mobility of PCBM is higher than that of the polymer.[27] Therefore, the observed low contrast in the sample with a PCBM weight fraction of 50% suggests the formation of PCBM crystals in between polymer domains. This speculation is further supported by the optoelectronic properties presented in the corresponding section. An increase in the average scattering intensity is found for a PCBM content higher than 50%, which is attributed to a better phase separated morphology. As a consequence, in combination with the findings from the analysis of the 2D GISANS patterns, we estimate a phase transition process from a lamellar- into a cylindrical-morphology occurred within the diblock copolymer P3HT-*b*-PS at a PCBM weight fraction higher than 50%. More details are explained in the following section. However, with respect to the important exciton dissociation process length scales on the order of 10 nm are important in BHJ films and scattering features which originate from smaller domains, i.e. at larger q_y values, need to be analyzed.[63-65]

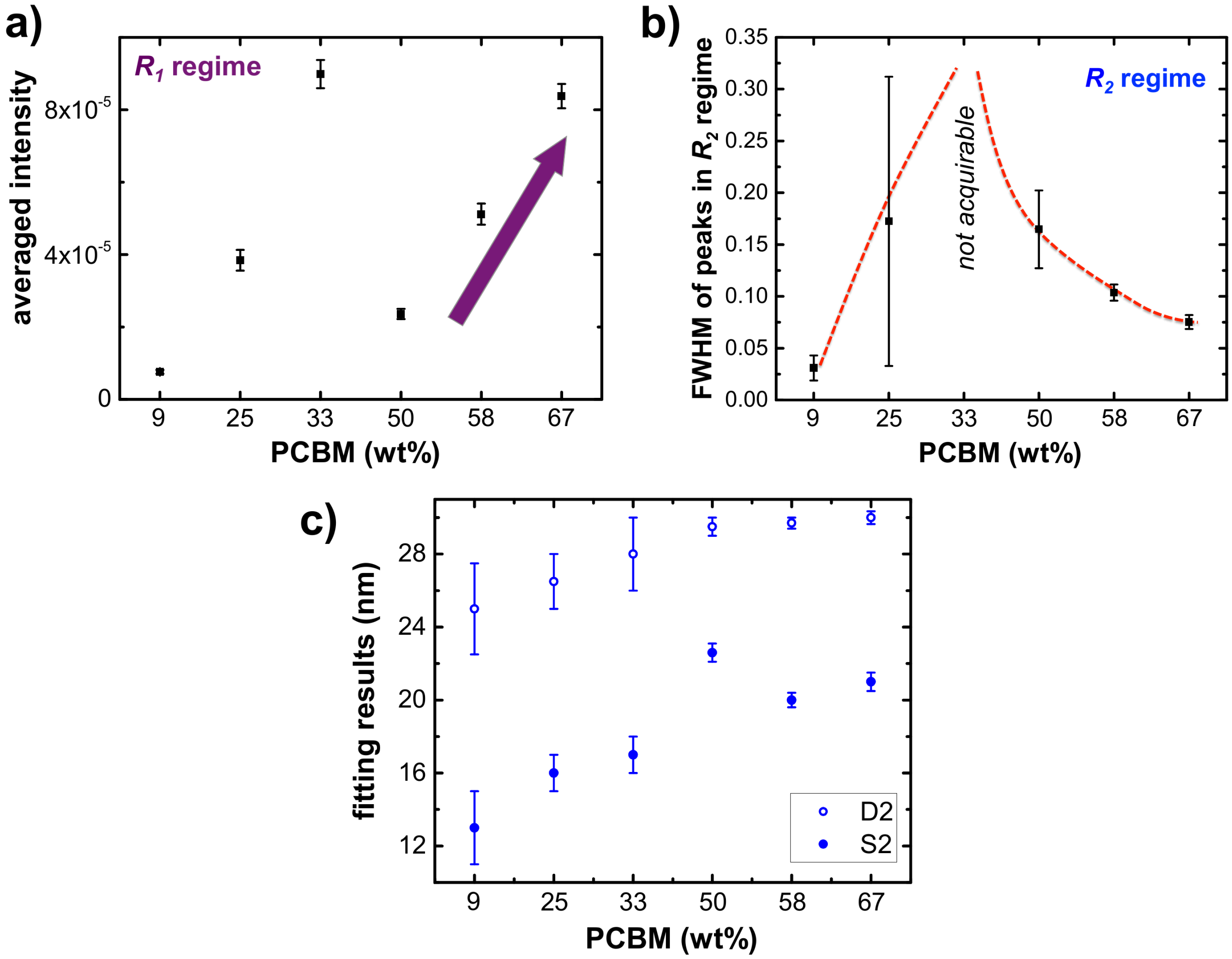

Fig. 6. (a) Average scattering intensities (intensity for each sample is normalized to 1 hr counting time) for the hundred nanometer scale domains (R_1 regime in Fig. 5b) are to explain contrast changes caused by changing the blend ratio. The contrast development in samples contain PCBM weight fraction above 50% is highlight with a purple arrow. (b) Full width at half-maximum (FWHM) of the scattering peaks in R_2 regime in Fig. 5b for blend films with different PCBM weight fractions. (c) The extracted morphological parameters for the ten nanometer scale substructure in R_2 regime in Fig. 5b (S represents the domain size whereas d represent the distance between different domains). The error bars describe the scale length distribution applied in the fitting.

For the film with the lowest PCBM weight fraction of 9% (orange curve in Fig. 5b) a form factor contribution in the intensity is seen at $q_y \approx 0.2$ nm^{-1} indicating a domain size of 13 ± 2 nm, which is in good agreement with the AFM PSD results (Fig. S3). Based on the pristine diblock copolymer molecular structure, we estimate the diblock copolymer distributes in a lamellar morphology at this PCBM weight fraction. For the samples with higher PCBM content, the shoulder-like peak at $q_y \approx 0.2$ nm^{-1} becomes broader and weaker till a PCBM weight fraction of 33% is reached, while upon further loading with PCBM, the peak returns to be more pronounced (indicated by the black arrow in Fig. 5b). The degree of order in the block copolymer determines the full width at half-maximum (FWHM) of the scattering peaks. A system comprising a better segregation and higher degree of order possesses a smaller value of the FWHM.[29,66,67] Using Gaussian peaks to represent the scattering features locate at the R_2 region, the revealed FWHM values in Fig. 6b indicate that the ordering of P3HT-*b*-PS decreases from 9% to 33%. This result is consistent with the observation in GI-XRD that a kinetically favored mechanism effects samples with PCBM weight fractions of 25% and 33%. For the higher PCBM weight fractions above 50%, an increased segregation strength associated with a better spatial correlation order is observed. As seen in Fig. 3a, the P3HT crystallinity decreases with increasing the PCBM content from 50% to 67%. Herein, we hypothesize that the better-ordered hexagonally packed cylinder morphology in the films containing a higher PCBM content results from the beneficial impact of the P3HT-*b*-PS microphase separation. A similar result was observed in binary blends of diblock copolymer and homopolymer.[68] However, the gyroid nanostructure is speculated to be bypassed in the present blend films due to the weak driving force upon morphology transformation.[69] The domain size increases from 13 ± 2 nm to 21 ± 0.5 nm for a PCBM content increasing from 9% to 67%. Thus, the domain size slightly grows with increasing PCBM content. The dependence of the block copolymer domain swelling on the PCBM content is evidence that the PCBM is incorporated in the P3HT-*b*-PS.[29] Moreover, it is due to the larger interface area provided by the hexagonally packed cylinder lattice in the sample with 67% PCBM as compared to the lamellar morphology found in the sample with 9% PCBM. This hypothesis is further supported by our calculation that the PCBM domains tend to leave the hexagonal lattice for sample with an increased PCBM weight fraction from 58% to 67% (see supporting information, Fig. S7). Alongside, distances between the copolymer domains increase with higher PCBM content as well.

A schematic description of the local film morphology is illustrated in Fig. 7. Four different stages are identified: (1) At the lowest PCBM content (9%) PCBM preferentially interacts with the PS domains. The P3HT block is well crystallized whereas no PCBM crystallites are identifiable as supported by the GI-XRD measurement. The blend film at this composition preserves a lamellar morphology in accordance to the pure diblock copolymer, which is driven by the crystallization of the P3HT block; (2) Upon increasing the PCBM content (25% and 33%) the PS domains swell to accommodate the PCBM. The nanoscale order of the block copolymer P3HT-*b*-PS decreases (Fig. 6b) associated with the kinetically favored face-on P3HT orientation found in GI-XRD; (3) With further increasing the PCBM content (50% and 58%), a phase transition of the diblock copolymer occurs. In addition, due to excess PCBM larger PCBM domains emerge and position in between the diblock copolymer domains, as the GISANS contrast diminishes when increasing the PCBM weight fraction from 33% to 50% (Fig. 6a); (4) For the highest PCBM weight fraction (67%), the cylindrical diblock copolymer distributes in a well ordered hexagonal lattice (Fig. 4f) and better segregated PCBM domains formed on the mesoscale (Fig. 6a).

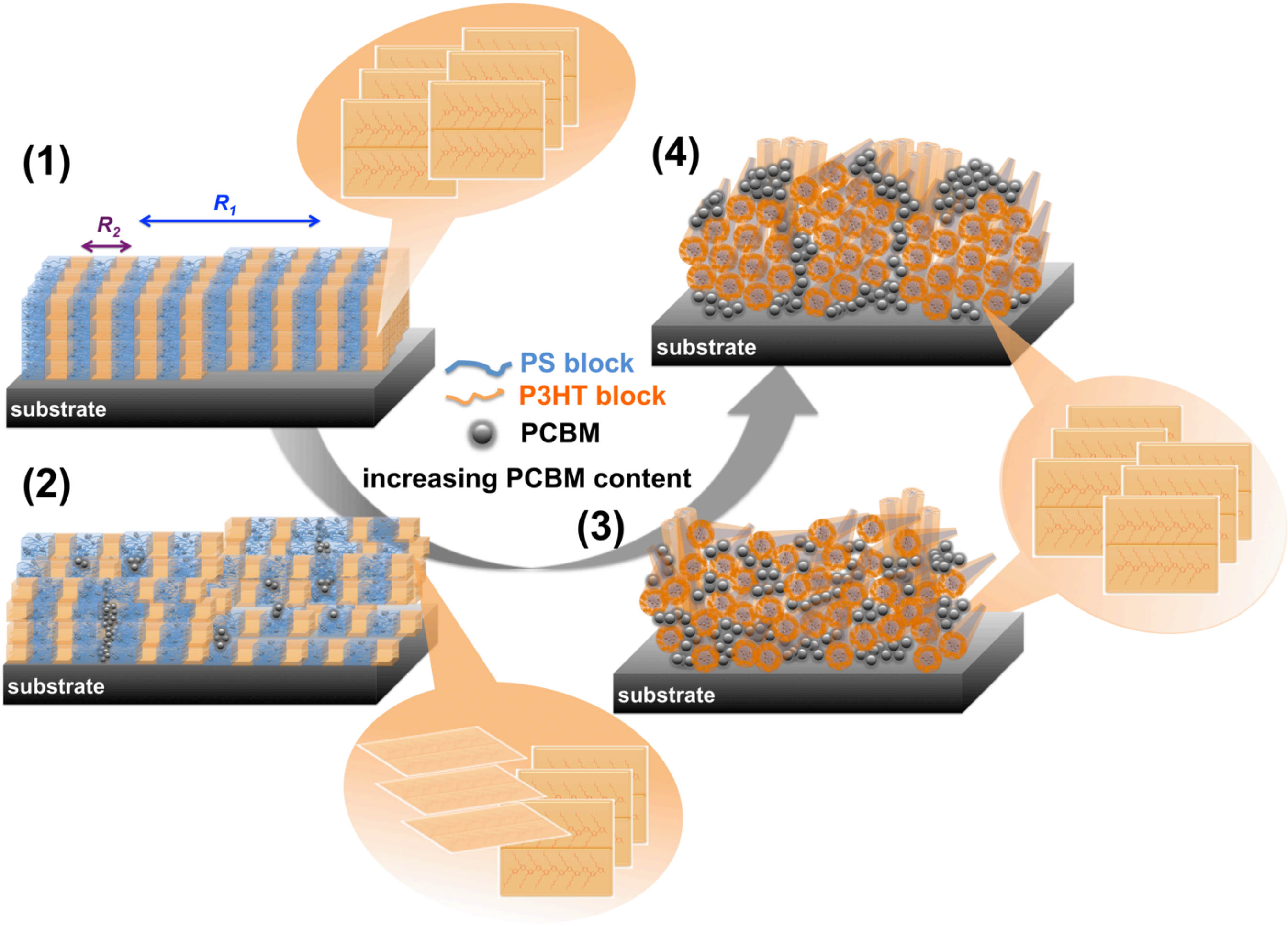

Fig. 7. Schematic illustration of the morphology transformation in P3HT-*b*-PS:PCBM films. The two blocks of the diblock copolymer are depicted in orange (P3HT) and blue (PS) whereas PCBM is shown as grey spheres. In addition, P3HT crystalline orders are depicted in a zoom-in view. Both the (1) initial lamellar microphase separation structure of the diblock copolymer and the P3HT edge-on orientation are perturbed by the (2) incorporation of PCBM in the PS domains. (3) Films with higher PCBM content undergo a transformation of the microphase separation structure into a less ordered cylinder morphology. More specifically, the kinetically favored P3HT face-on orientation disappears. (4) A further increase in PCBM content gives rise to a better segregated domain structure on the hundred nanometer scale as well as a hexagonally packed cylinder morphology.

3.4 Optoelectronic properties

In order to deepen the findings from GI-XRD, we characterize the crystalline quality of all blend films by means of absorbance and photoluminescence spectroscopy. In Fig. 8a, the absorbance data of all six blend films are shown. The absorbance peak at around 335 nm is attributed to PCBM. It increases in intensity with increasing PCBM weight fraction. The absorbance features above 400 nm are dominated by the P3HT block of the diblock copolymer P3HT-*b*-PS. Besides the main absorbance peak of P3HT at around 500 nm, two additional absorbance peaks appear at around 550 nm and around 605 nm, reflecting the vibronic 0-0 and 0-1 transitions, respectively.[56,70] The position of the P3HT main absorbance peak shifts towards smaller wavelengths with increasing PCBM content. Such shift is indicative of an increase in the energy band gap, which means that the crystallinity of P3HT is disturbed by PCBM addition in good agreement with the observations from GI-XRD. A reasonable explanation is to consider that the PCBM molecules are rapidly crystallizing upon thermal annealing, which competes the crystallization of the P3HT block in the diblock copolymer P3HT-*b*-PS.[27] From literature, it is also reported that the PCBM molecules not only disrupt the P3HT interchain π-π stacking, but also effect the conjugation length of the P3HT chains (the intrachain order).[71] To have a deeper understanding about the relationship between the different blend ratios and the obtained interchain coupling, further analysis of the absorbance data is carried out. Within the H aggregate model (equation 1) we determine the free exciton bandwidths (W)[72]

In

$$\frac{A_{0-0}}{A_{0-1}} = \frac{n_{0-0}}{n_{0-1}}\left(\frac{1-0.24^{W}/_{E_p}}{1+0.073^{W}/_{E_p}}\right)^2 \qquad (1)$$

$n_{0\text{-}i}$ are the real part of the refractive index at the corresponding absorption bands and E_p is a constant value describing the phonon energy of the electronically excited state. Assuming a refractive index ratio of around 1, equation 1 can be rewritten to

$$\boldsymbol{W = \frac{E_p(1-\sqrt{\frac{A_{0-0}}{A_{0-1}}})}{0.073\sqrt{\frac{A_{0-0}}{A_{0-1}}}+0.24}} \qquad (2)$$

which means the free exciton bandwidth (W) is inversely proportional to the ratio of the 0-0 and 0-1 absorbance. Using $Ep = 0.18$ eV,[72] the obtained results from using equation 2 are shown in Fig. 8b. A small exciton bandwidth indicates a large conjugation length.[71] For the studied P3HT-*b*-PS:PCBM blend system, the conjugation length of the P3HT block is decreasing from a PCBM weight fraction of 9% till 33%, while increasing upon further loading of PCBM content up to a weight fraction of 67%. These results are in good agreement with the observations concerning the P3HT (100) reflection in the GI-XRD measurements (Fig. 3a). Moreover, the obtained values of W are around 50 meV for sample contains a PCBM weight fraction larger than 50%, which means that the P3HT crystalline order fully meets the requirement for well working solar cells devices.[21]

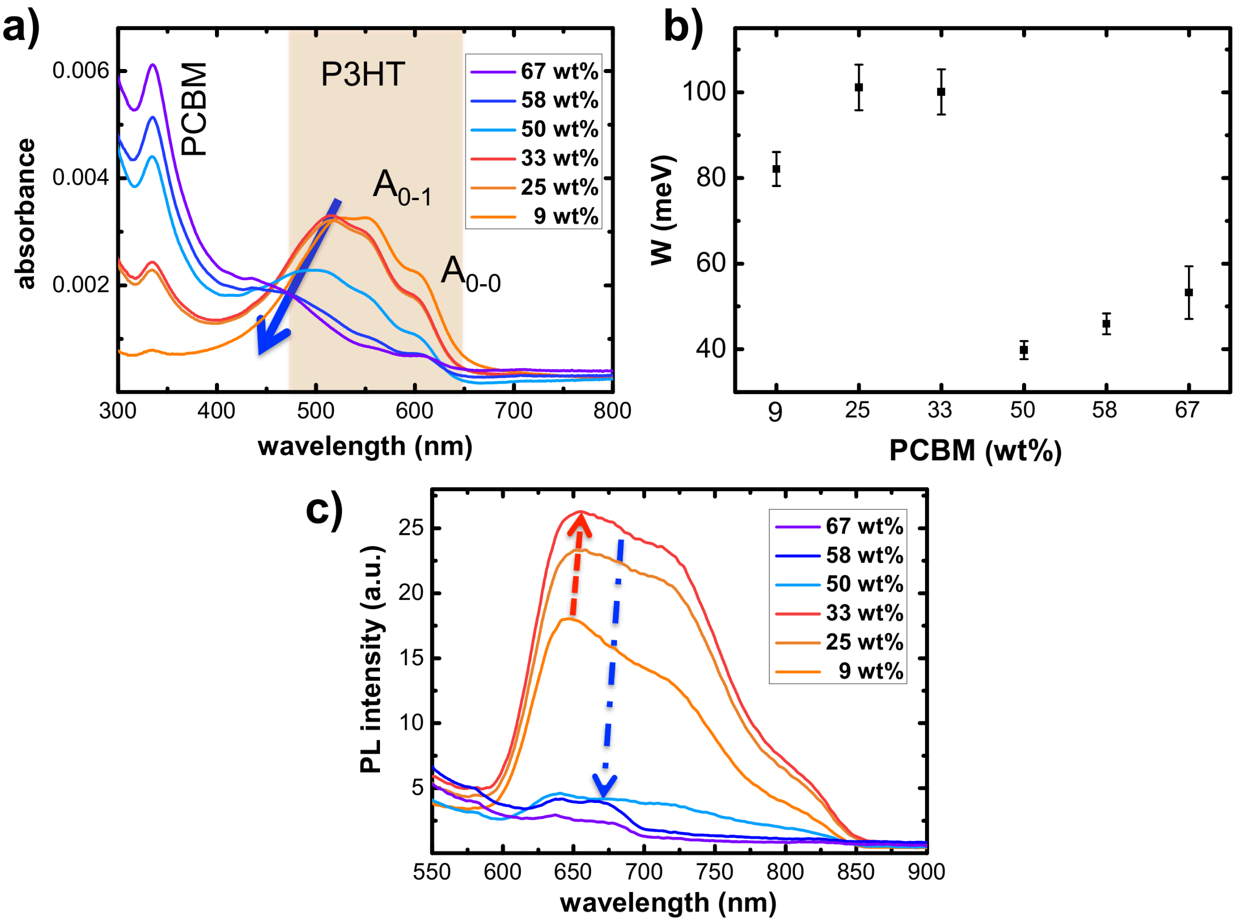

Fig. 8. (a) Wavelength dependent absorbance spectra of P3HT-b-PS:PCBM blend films with blend ratios as indicated. A blue shift of the P3HT main absorption peak is highlighted. (b) Exciton bandwidth W plotted as function of PCBM weight fraction. (c) Photoluminescence (PL) spectra of P3HT-b-PS:PCBM blend films with blend ratios as indicated.

In Fig. 8c, photoluminescence (PL) measurements show the PL intensity of the exciton radiative decay within the P3HT block of the diblock copolymer P3HT-*b*-PS. Apart from the PCBM weight fraction of 25% and 33%, an increased quenching of the PL intensity is found for increasing PCBM content, which is promising for real photovoltaic device as this indicates a successful exciton splitting. The seen high PL intensities are indicative of well phase separated P3HT and PCBM domains. In addition, a large disorder of the P3HT chains as found in the GI-XRD would also lead to increased PL intensities for samples with 25% and 33% PCBM content.[73] The PL intensity in the sample with a PCBM weight fraction of 50% is five times lower as compared to the sample with 33% PCBM. Since the P3HT block weight fraction decreases by only 10% in the 50% sample as compared to 33% sample, the corresponding five times stronger PL quenching may be ascribed as a fast photoinduced charge transfer between the P3HT electron donor and PCBM electron acceptor. This hypothesis is consistent with the GISANS results that PCBM crystals are distributing among the polymer domains on the mesoscale in sample contains a PCBM weight fraction of 50%.

4. Conclusions

In general diblock copolymers are promising candidates for the fabricating of high performance microelectronic devices according to their intrinsic characteristics of forming well-ordered nanoscale structures due to microphase separation. We study the blend P3HT-*b*-PS:PCBM with respect to the morphology as well as to the optoelectronic properties. Different blend ratios in terms of a PCBM content varying from 9% up to 67% are probed. Our findings indicate that the preferential interaction between the PS block and PCBM causes a morphology transformation of the P3HT-*b*-PS film from a lamellar morphology (sample with a PCBM content of 9%) into a hexagonally packed cylinder morphology (sample with a PCBM content of 67%). GISANS reveals that better segregated domains on the hundred nanometer scale are formed for samples with a higher PCBM content. Due to the chosen diblock copolymer molecular weight, the micro-phase separation induced domain size distributes on a length scale of around ten to twenty nanometers for the studied blend ratios. Both, domain size and domain distance, are increasing upon loading more PCBM into the BHJ films. Interestingly, we also demonstrate that, the P3HT crystallite orientation is co-alternating alongside with the mesoscale morphology transformation. For intermediate PCBM content a P3HT face-on molecular orientation arise, whereas for low and high PCBM content the edge-on orientation is present. With respect to a potential optoelectronic application, the observed absorbance and photoluminescence results demonstrate that the changes of the film morphology have clear effects on the optoelectronic properties. Combining all our observations, we estimate that blend films with a PCBM weight fraction higher than 50% appear promising concerning the application of the studied blend films in organic solar cells. However, an optimization of the diblock copolymer molecular weight might be required before making devices with P3HT-*b*-PS:PCBM blend active layers.

Acknowledgements

PMB acknowledges funding from the Excellence cluster "Nanosystems Initiative Munich" (NIM) and from TUM.solar in the frame of the Bavarian Collaborative Research Project "Solar technologies go Hybrid" (SolTec). Armin Kriele is acknowledged for providing kindly help in GI-XRD measurement. Dr. Sabine Pütter is acknowledged for providing kindly help in AFM measurement.

Appendix A. Supplementary data

References

[1] J.Y. Cheng, A.M. Mayes, C.A. Ross, Nat. Mater. 3 (2004) 823-828.
[2] J.Y. Cheng, C.A. Ross, H.I. Smith, E.L. Thomas, Adv. Mater. 18 (2006) 2505-2521.
[3] J. Bang, U. Jeong, D.Y. Ryu, T.P. Russell, C.J. Hawker, Adv. Mater. 21 (2009) 4769-4792.
[4] L. Leibler, Macromolecules 13 (1980) 1602-1617.
[5] F.S. Bates, G.H. Fredrickson, Phys. Today 52 (1999) 32-38.
[6] H.-C. Kim, S.-M. Park, W.D. Hinsberg, Chem. Rev. 110 (2010) 146-177.
[7] M.C. Orilall, U. Wiesner, Chem. Soc. Rev. 40 (2011) 520-535.
[8] P.P. Soo, B. Huang, Y.-I. Jang, Y.-M. Chiang, D. R. Sadoway, A. M. Mayes, J. Electrochem. Soc. 146 (1999) 32-37.
[9] E. Metwalli, M. Rasool, S. Brunner, P. Müller-Buschbaum, ChemPhysChem, 16 (2015) 2882-2889.
[10] K. Kataoka, A. Harada, Y. Nagasaki, Adv. Drug Delivery Rev. 47 (2001) 113-131.
[11] Y.-C. Tseng, S. B. Darling, Polymers 2 (2010) 470-489.
[12] F. S. Bates, Science, 251 (1991) 898-905.
[13] G. H. Fredrickson, F. S. Bates, Annu. Rev. Mater. Sci. 26 (1996) 501-550.
[14] H.-A. Klok, S. Lecommandoux, Adv. Mater. 13 (2001) 1217-1220.
[15] S.-H. Lin, C.-C. Hoa, W.-F. Su, Soft Matter 8 (2012) 4890-4893.
[16] B. D. Olsen, R. A. Segalman, Macromolecules 40 (2007) 6922-6929.
[17] N. Sary, L. Rubatat, C. Brochon, G. Hadziioannou, J. Ruokolaonen, R. Mezzenga, Macromolecules 40 (2007) 6990-6997.
[18] C. C. Ho, Y. H. Lee, C. A. Dai, R. A. Segalman, W. F. Su, Macromolecules 42 (2009) 4208-4219.
[19] R. H. Friend, R. W. Gymer, A. B. Holmes, J. H. Burroughes, R. N. Marks, C. Taliani, D. D. C. Bradley, D. A. Dos Santos, J. L.Brédas, M. Lögdlund, W. R. Salaneck, Nature 397 (1999) 121-128.
[20] M. A. Ruderer, P. Müller-Buschbaum, Soft Matter 7 (2011) 5482-5493.

[21] W. Wang, S. Guo, E. M. Herzig, K. Sarkar, M. Schindler, D. Magerl, M. Philipp, J. Perlich, P. Müller-Buschbaum, J. Mater. Chem. A 4 (2016) 3743-3753.

[22] U. Sherf, S. Adamczyk, A. Gutacker, N. Koenen, Macromol. Rapid Commun. 30 (2009) 1059-1065.

[23] D. Deribew, E. Pavlopoulou, G. Fleury, C. Nicolet, C. Renaud, S.-J. Mougnier, L. Vignau, E. Cloutet, C. Brochon, F. Cousin, G. Portale, M. Geoghegan, G. Hadziioannou, Macromolecules 46 (2013) 3015-3024.

[24] W. Ma, A. Gopinathan, A.J. Heeger, Adv. Mater. 19 (2007) 3656-3659.

[25] M.-Y. Chiu, U.-S. Jeng, M.-S. Su, K.-H. Wei, Macromolecules 43 (2010) 428-432.

[26] C. R. McNeill, B. Watts, L. Thomsen, H. Ade, N. C. Greenham, P. C. Dastoor, Macromolecules 40 (2007) 3263-3270.

[27] R. Dattani, J.H. Bannock, Z. Fei, R.C.I. MacKenzie, A.A.Y. Guilbert, M.S.Vezie, J. Nelson, J.C. de Mello, M. Heeney, J.T. Cabral, A.J. Nedoma, J. Mater. Chem. A 2 (2014) 14711-14719.

[28] V. Gernigon, P. Lévêque, F. Richard, N. Leclerc, C. Brochon, C.H. Braun, S. Ludwigs, D.V. Anokhin, D.A. Ivanov, G. Hadziioannou, T. Heiser, Macromolecules 46 (2013)8824-8831.

[29] Y. Lin, J.A. Lin, Q. Wei, S.C.B. Mannsfeld, A.L. Briseno, J.J. Watkins, Chem. Mater. 24 (2012) 622-632.

[30] P. Müller-Buschbaum, Eur. Phys. J. E: Soft Matter Biol. Phys. 12 (2003) 443-448.

[31] A.V. Feoktystov, H. Frielinghaus, Z. Di, S. Jaksch, V. Pipich, M.-S. Appavou, E. Babcock, R. Hanslik, R. Engels, G. Kemmerling, H. Kleines, A. Ioffe, D. Richter, T. Brückel, J. Appl. Crystallogr. 48 (2015) 61-70.

[32] Heinz Maier-Leibnitz Zentrum, et al., J. Large-Scale Res. Facil. 1 (2015) A28.

[33] H. Zhong, X. Yang, B. deWith, J. Loos, Macromolecules 39 (2006) 218-223.

[34] B. Watts, W.J. Belcher, L. Thomsen, H. Ade, P.C. Dastoor, Macromolecules 42 (2009) 8392-8397.

[35] X. Yang, J. Loos, S.C. Veenstra, W.J.H. Verhees, M.M. Wienk, J.M. Kroon, M.A.J. Michels, R.A.J. Janssen, Nano Lett. 5 (2005) 579-583.

[36] S. Berson, R. De Bettignies, S. Bailly, S. Guillerez, Adv. Funct. Mater. 17 (2007) 1377-1384.

[37] V. Ho, B.W. Boudouris, B.L. McCulloch, C.G. Shuttle, M. Burkhardt, M.L. Chabinyc, R.A. Segalman, J. Am. Chem. Soc. 133 (2011) 9270-9273.

[38] B.W. Boudouris, C.D. Frisbie, M.A. Hillmyer, Macromolecules 43 (2010) 3566-3569

[39] E.C. Davidson, B.S. Beckingham, V. Ho, R.A. Segalman, J. Polym. Sci. Part B: Polym. Phys., 54 (2016) 205-215.

[40] C.-W. Chu, H. Yang, W.-J. Hou, J. Huang, G. Li, Y. Yang, Appl. Phys. Lett. 92 (2008) 103306.

[41] H. Yang, S.W. LeFevre, C.Y. Ryu, Z. Bao, Appl. Phys. Lett. 90 (2007) 172116.

[42] D.M. Delongchamp, B.M. Vogel, Y. Jung, M.C. Gurau, C.A. Richter, O.A. Kirillov, J. Obrzut, D.A. Fischer, S. Sambasivan, L.J. Richter, E.K. Lin, Chem. Mater. 17 (2005) 5610-5612.

[43] Y. Lin, V.K. Daga, E.R. Anderson, S.P. Gido, J. J. Watkins, J. Am. Chem. Soc. 133 (2011) 6513-6516.

[44] Z. Sun, K. Xiao, J.K. Keum, X. Yu, K. Hong, J. Browning, I.N. Ivanov, J. Chen, J. Alonzo, D. Li, B.G. Sumpter, E.A. Payzant, C.M. Rouleau, D.B. Geohegan, Adv. Mater. 23 (2011) 5529-5535.

[45] N.D. Treat, M.A. Brady, G. Smith, M.F. Toney, E.J. Kramer, C.J. Hawker, M. L. Chabinyc, Adv. Energy Mater. 1 (2011) 145-145.

[46] D. Chen, F. Liu, C. Wang, A. Nakahara, T.P. Russell, Nano Lett. 11 (2011) 2071-2078.

[47] P. Müller-Buschbaum, Polymer J. 45 (2013) 34-42.

[48] W.-R. Wu, U.-S. Jeng, C.-J. Su, K.-H. Wei, M.-S. Su, M.-Y. Chiu, C.-Y. Chen, W.-B. Su, C.-H. Su, A.-C. Su, ACS Nano 5 (2011) 6233-6243.

[49] Y.-C. Huang, C.-S. Tsao, C.-M. Chuang, C.-H. Lee, F.-H. Hsu, H.-C. Cha, C.-Y. Chen, T.-H. Lin, C.-J. Su, U.-S. Jeng and W.-F. Su, J. Phys. Chem. C 116 (2012) 10238-10244.

[50] D.-M. Smilgies, R. Li, G. Giri, K.W. Chou, Y. Diao, Z. Bao, A. Amassian, Phys. Status Solidi RRL 7 (2013) 177-179.

[51] K. Chou, B. Yan, R. Li, E. Li, K. Zhao, D. Anjum, S. Alvarez, R. Gassaway, A. Biocca, S. Thoroddsen, A. Hexemer, A. Amassian, Adv. Mater. 25 (2013) 1923-1929.

[52] H.-C. Liao, C.-S. Tsao, Y.-T. Shao, S.-Y. Chang, Y.-C. Huang, C.-M. Chuang, T.-H. Lin, C.-Y. Chen, C.-J. Su, U. S. Jeng, Y.-F. Chen, W.-F. Su, Energy Environ. Sci. 6 (2013) 1938-1948.

[53] P. Muller-Buschbaum, Adv. Mater. 26 (2014) 7692-7709.

[54] P. Müller-Buschbaum, Eur. Polym. J. 81 (2016) 470-493.

[55] B.A. Collins, E. Gann, L. Guignard, X. He, C.R. McNeill, H. Ade, J. Phys. Chem. Lett. 1 (2010) 3160-3166.

[56] M.A. Ruderer, R. Meier, L. Porcar, R. Cubitt, P. Müller-Buschbaum, J. Phys. Chem. Lett. 3 (2012) 683-688.

[57] Y. Yoneda, Phys. Rev. 131 (1963) 2010-2013.

[58] P. Müller-Buschbaum, Anal. Bioanal. Chem. 376 (2003) 3-10.

[59] P. Müller-Buschbaum, in *Applications of Synchrotron Light to Scattering and Diffraction in Materials and Life Sciences*, ed. M. Gomez, A. Nogales, M. C. Garcia-Gutierrez, T.A. Ezquerra, Springer, Berlin, 2009, chapter 3, 61-86.

[60] D. Magerl, M. Philipp, E. Metwalli, P. Gutfreund, X.P. Qiu, F.M. Winnik, P. Müller-Buschbaum, ACS Macro Lett. 4 (2015) 1362-1365.

[61] J.S. Higgins, H.C. Benoit, *Polymers and Neutron Scattering*, Oxford University Press Inc., New York, 1997.

[62] R.J. Roe, *Methods of X-ray and Neutron Scattering in Polymer Science*, Oxford University Press, New York, 2000.

[63] S. Günes, H. Neugebauer, N.S. Sariciftci, Chem. Rev. 107 (2007) 1324-1338.

[64] P.E. Shaw, A. Ruseckas, I.D.W. Samuel, Adv. Mater. 20 (2008) 3516-3520.

[65] O.V. Mikhnenko, H. Azimi, M. Scharber, M. Morana, P.W.M. Blom, M.A. Loi, Energy Environ. Sci. 5 (2012) 6960-6965.

[66] I. Tokarev, R. Krenek, Y. Burkov, D. Schmeisser, A. Sidorenko, S. Manko, M. Stamm, Macromolecules 38 (2005) 507-516.

[67] V.R. Tirumala, A. Romang, S. Agarwal, E.K. Lin, J.J. Watkins, Adv. Mater. 20 (2008) 1603-1608.

[68] K.I. Winey, E.L. Thomas, L.J. Fetters, J. Chem. Phys. 95 (1991) 9367-9375.

[69] M.E. Vigild, K. Almdal, K. Mortensen, I.W. Hamley, J.P.A. Fairclough, A.J. Ryan, Macromolecules 31 (1998) 5702-5716.

[70] F.C. Spano, J. Clark, C. Silva, R.H. Friend, J. Chem. Phys. 130 (2009) 074904.

[71] Y. Gao, T.P. Martin, E.T. Niles, A.J. Wise, A.K. Thomas, J.K. Grey, J. Phys. Chem. C 114 (2010) 15121-15128.

[72] J. Clark, C. Silva, R.H. Friend, F.C. Spano, Phys. Rev. Lett. 98 (2007) 206406.

[73] S.S. van Bavel, M. Bärenklau, G. de With, H. Hoppe, J. Loos, Adv. Funct. Mater. 20 (2010) 1458-1463.